Journal of Electron Microscopy **50(3)**: 251–263 (2001)

Full-length paper

Nanocrystal formation in hexagonal SiC after Ge$^+$ ion implantation

Ute Kaiser

Institut für Festkörperphysik, Friedrich-Schiller Universität, Jena 07743, Germany
E-mail: kaiser@pinet.uni-jena.de

Abstract High-resolution and analytical electron microscopy techniques are used to characterize Ge-implanted hexagonal SiC. After annealing the implanted samples at 1200°C, Ge is found to be located preferentially on interstitial sites. After annealing at 1600°C, small nanocrystals of strained cubic and hexagonal (or faulted cubic) Ge and Ge Si form. Occasionally, hexagonal (or faulted cubic) Si nanocrystals are observed also.

Keywords Ge implantation, Bloch wave calculation, ALCHEMI, nanocrystal formation, HRTEM, faulted GeSi nanocrystals

Received 20 February 2001, accepted 27 March 2001

Introduction

The optical properties of bulk Si and Ge are modified significantly if the material is manipulated at the nanometre scale. In particular, the growth of Si and Ge nanostructures constitutes a promising approach for the development of Si-based light emitting devices [1,2]. Small Ge and Si crystals are expected to show quantum size effects [3], and size-dependent photoluminescence has been measured for Ge nanocrystals embedded in amorphous SiO_2 [4]. SiC is a promising candidate for use as a matrix for Si and Ge nanocrystals because it has a large band gap, good ohmic contacts can be made with it [5] and it can be used in harsh environmental conditions.

Techniques such as molecular beam epitaxy [6] and ion implantation [7] can be used to fabricate nanostructures in SiC, in which effective interband transitions are expected for Ge dots [8]. Ion implantation has the advantage that it can be applied to an existing, well-defined SiC crystal, however, it may introduce point defects (interstitials and vacancies) [9,10], interstitial loops and defect clusters [11,12]. New polytypes [13–15], small precipitates [11] and voids [16,17] may form also. Subsequent annealing is then necessary to prevent the failure of the light-emitting device due to defect-induced non-radiative recombination [4,18–20]. Defect-enhanced diffusion is thought to be the key to a successful implantation-based nanostructure technology [13,21].

In order to understand the process of nanocrystal formation, it is important to determine whether the implanted ions are located on lattice sites or interstitial positions. A theoretical study of $Si_{1-x-y}Ge_xC_y$ has predicted that Ge should be located on Si sites in 3C-SiC [20], however, experimental confirmation of this prediction has not been presented. Whereas Al nanocrystals have been observed in 6H-SiC after Al-ion implantation and annealing at 1800°C [11], Ge nanocrystals have not been observed after implantation in SiC [13,22]. In this paper, the location of Ge atoms in high dose, high temperature Ge-implanted SiC annealed at 1200°C and 1600°C is determined.

Methods

Hexagonal SiC (6H and 4H) was implanted with $2 \times 10^{16}\,cm^{-2}$ 800 keV Ge$^+$ ions at 700°C, followed by annealing at either 1200 or 1600°C. Cross-sectional samples were prepared for transmission electron microscopy (TEM) using mechanical polishing, dimpling and low-angle Ar-ion milling. Microscopy was carried out in JEOL 3010, 2010F and 3000F TEMs using high-resolution (HR) imaging, energy dispersive X-ray (EDX) spectroscopy, electron energy-loss spectroscopy (EELS) and high-angle annular dark field (HAADF) imaging.

Bloch wave calculations for ALCHEMI (atom location by channelling enhanced microanalysis) were performed using the program of Tsuda and Tanaka [23], which incorporates the scattering factors of Doyle and Turner [24]. Experimental data were obtained using a Si (Li) EDX detector fitted with an atmospheric thin window and a pulse processor that could process X-rays above 0.7 keV. A liquid nitrogen-cooled Oxford Instruments double tilt holder was used to minimize contamination. Si, C and Ge signals were recorded at [01-10] and [12-30] for tilts of 1 / 2 g, 1 g, 3 / 2 g, 2 g and 5 / 2g with g = 0006

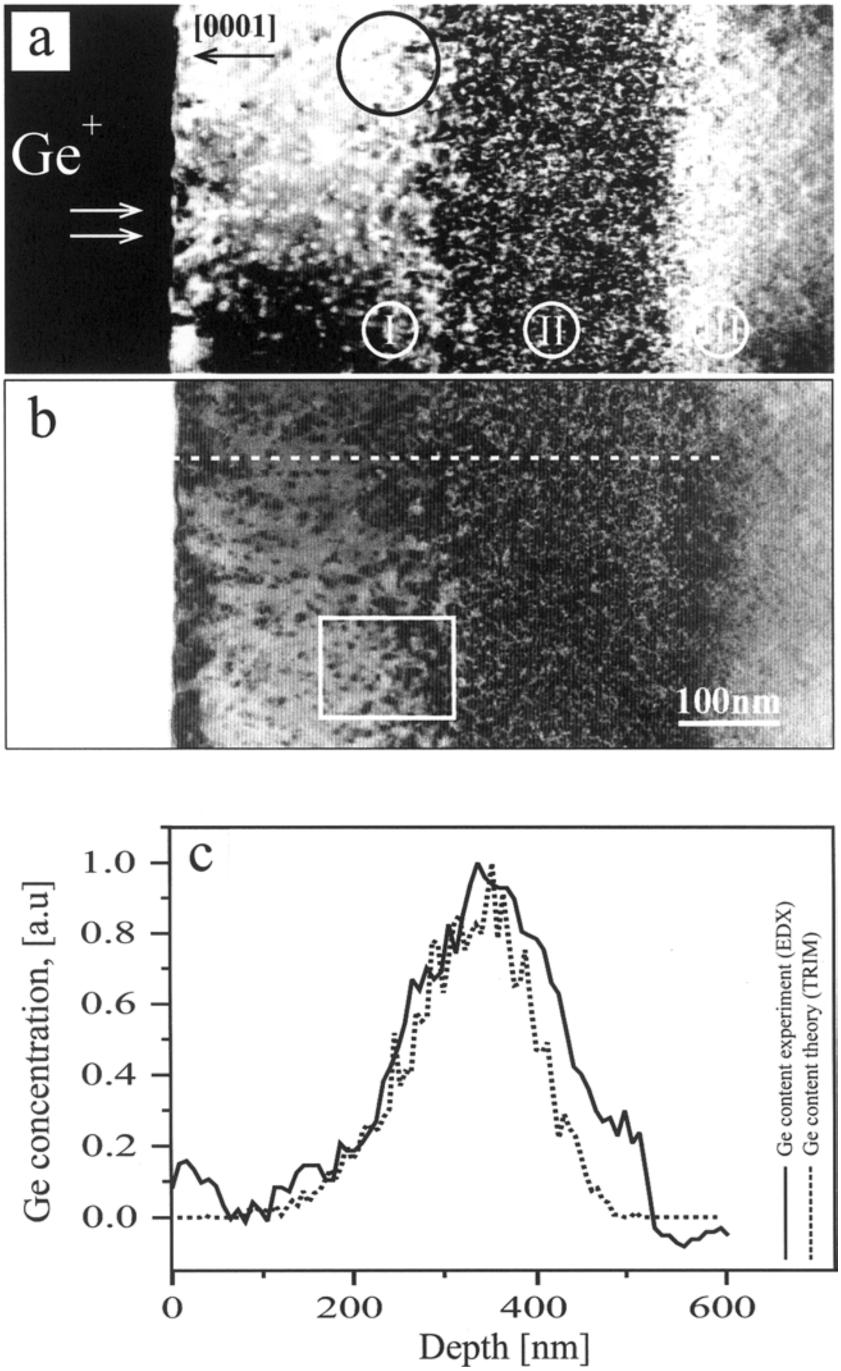

Fig. 1 (a) Bright-field and (b) dark-field images of SiC implanted with 2 × 10^{16} cm^{-2} Ge^+ at 800 eV and 700°C after annealing at 1200°C, showing diffusion-induced damage of the matrix differing in the regions marked I, II and III in (a). (c) EDX spectrum showing the distribution of Ge in the SiC matrix along the dashed white line marked in (b), alongside a TRIM calculation of the Ge content.

(parallel to c^*) and g = –2110 (perpendicular to c^*). Parallel illumination and thin specimen areas (between 70 and 90 nm) were used to produce strong and reproducible channelling effects. Five separate measurements were made at two regions to ensure reproducibility.

Digitally acquired HR images were analysed to determine lattice fringe spacings within nanocrystals using the Diffpack plug-in from Digital Micrograph [25]. The 0004 (0006) reflection of 4H-SiC (6H-SiC) was used to calibrate each HR micrograph accurately. The estimated accuracy of the measurements was 0.0001–0.005 nm for lattice spacings and 0.1–0.5° for interplanar angles [26].

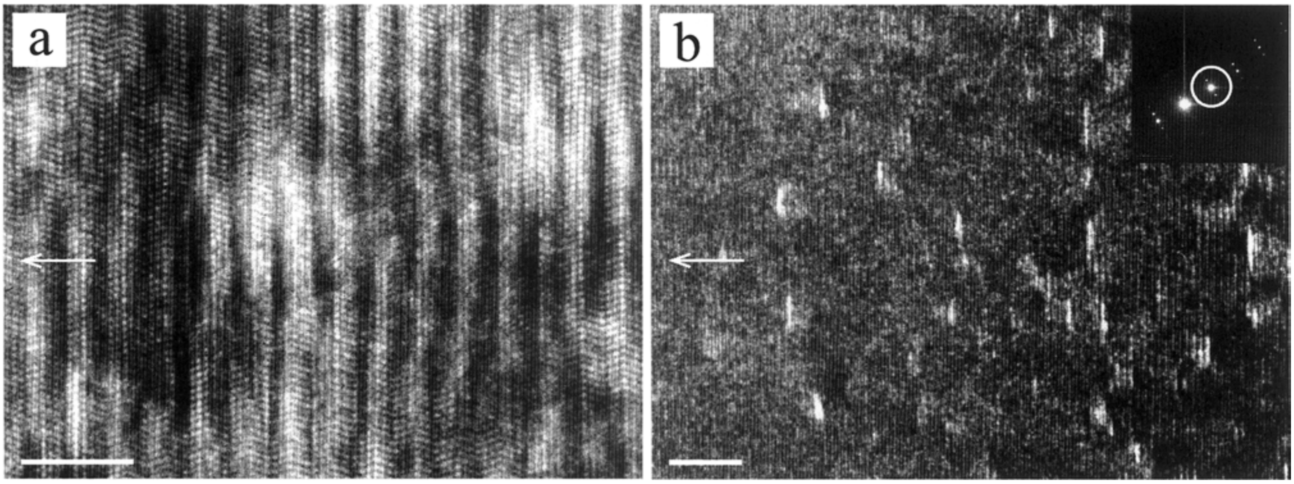

Fig. 2 (a) HR image from region I obtained inside the white rectangle in Fig. 1b showing bright-dark changes of the 6H-SiC contrast in small areas. (b) Tilted (see diffraction inserted) pattern dark-field image showing bright stripes. (The image is obtained from region I from the white rectangle in Fig. 1b.)

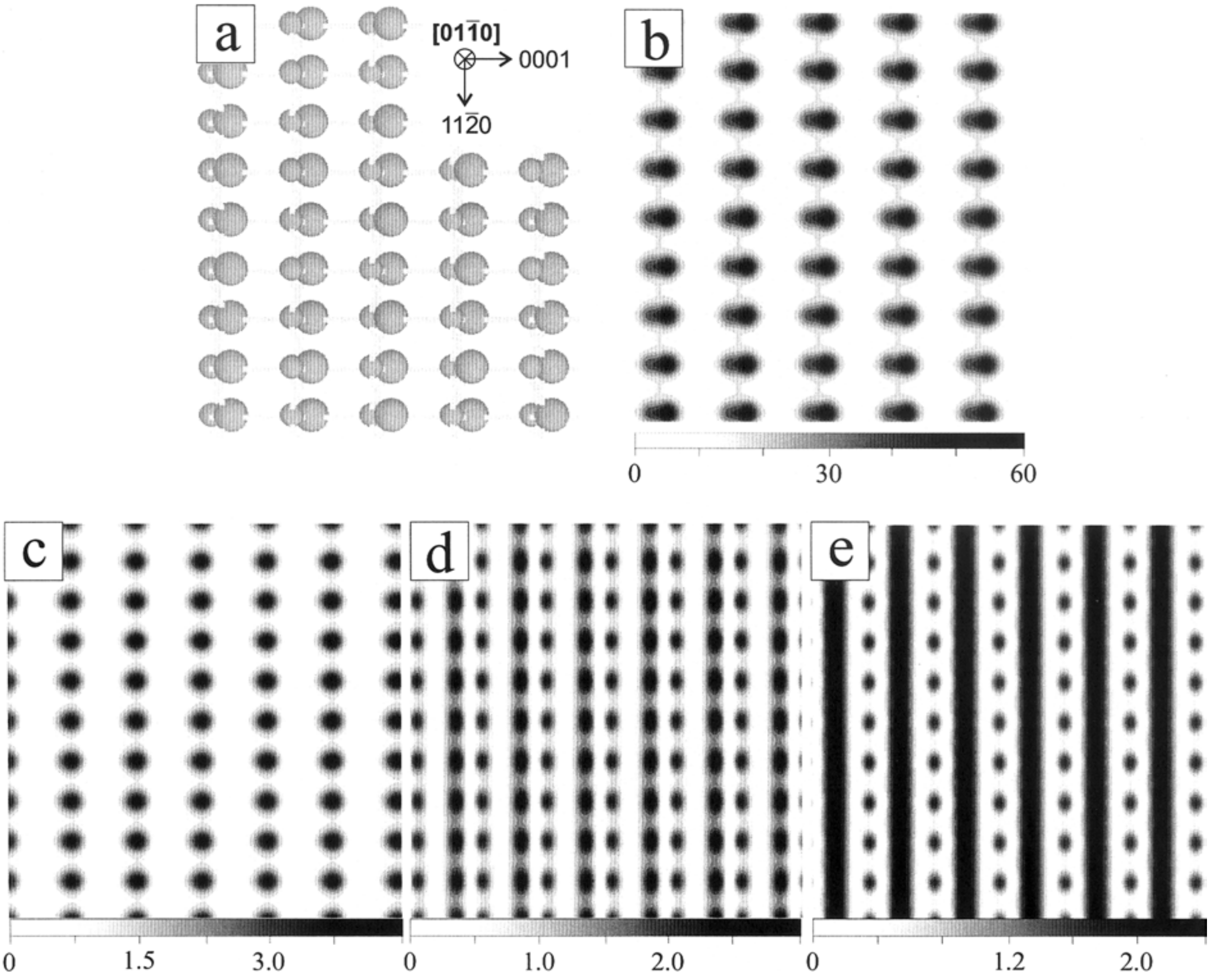

Fig. 3 (a) Projected structure of SiC along [01-10]; (b) projected potential; (c)–(e) electron-density distributions of Bloch waves for branches 1, 12 and 13, respectively. The electron density maxima are located on Si (branch 1), C (branch 12) or at interstitial positions (branch 13).

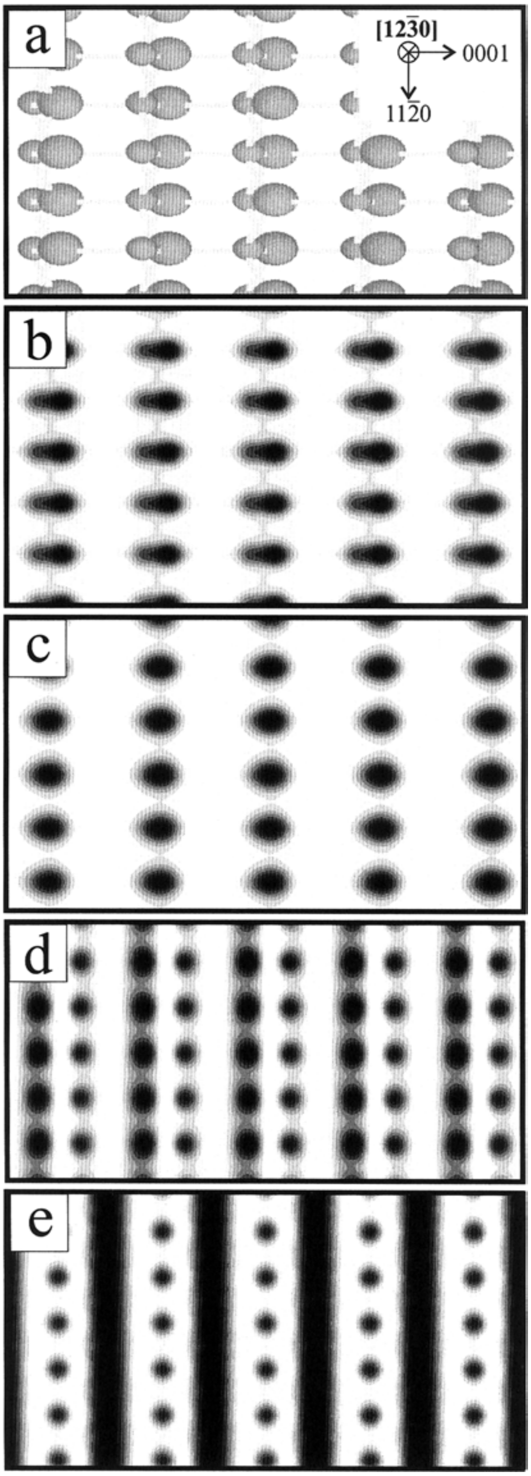

Fig. 4 (a) Projected structure of SiC along [12-30]; (b) projected potential; (c)-(e) electron-density distributions of Bloch waves for branches 1 (excitation intensity from 0 to 4.0), 12 (excitation intensity from 0 to 3.0) and 13 (excitation intensity from 0 to 3.0), respectively. The electron density maxima are located on Si (branch 1, (c)), C (branch 12, (d)) or at interstitial positions (branch 13, (e)).

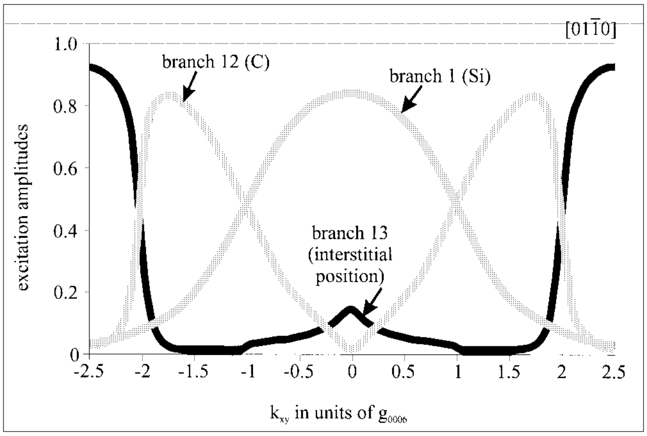

Fig. 5 Excitation amplitudes of Bloch states as a function of reciprocal lattice vector k_{xy} in units of g_{0006}.

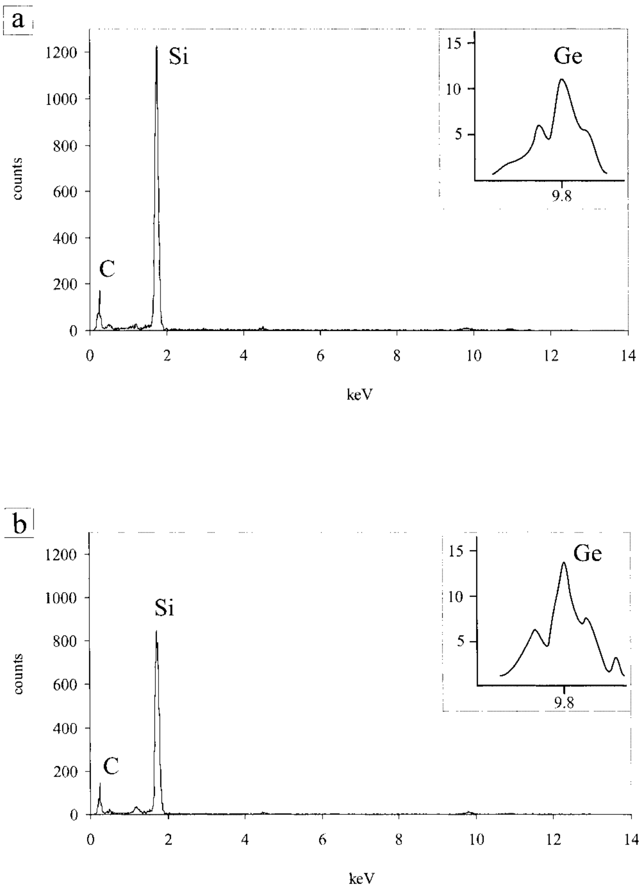

Fig. 6 EDX spectra obtained from the region encircled in Fig. 1a, (a) at [01-10] and (b) at a tilt of 2.5 g_{0006} from [01-10].

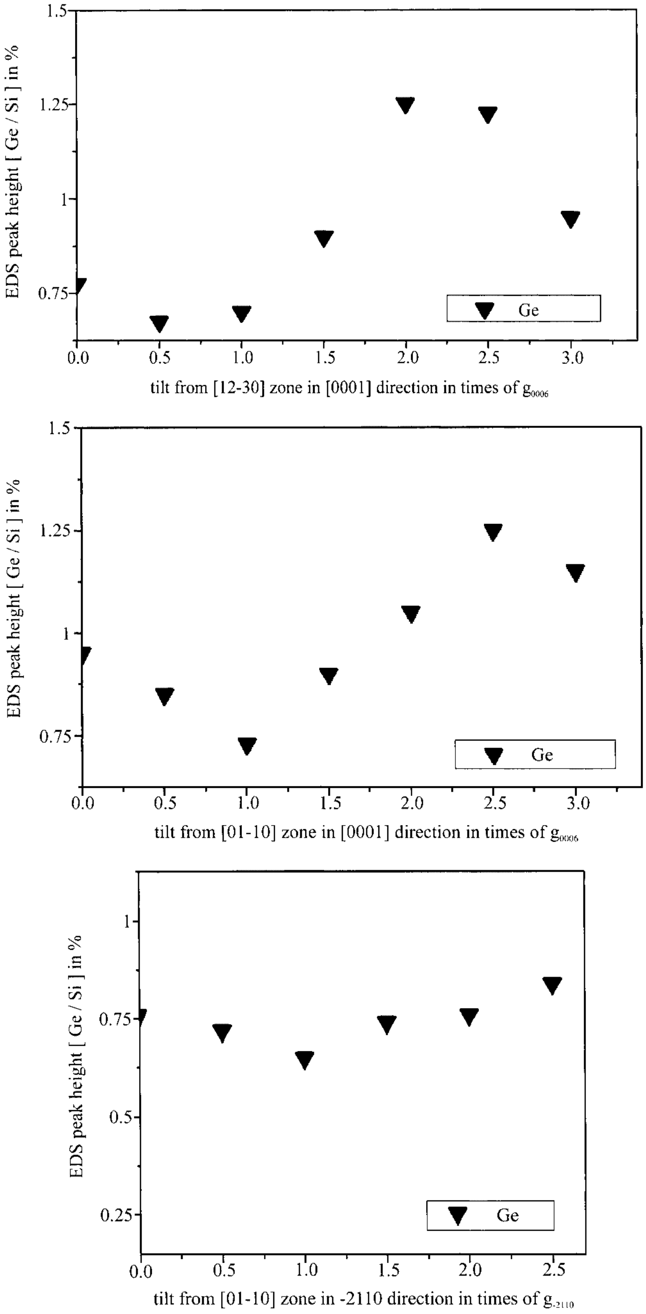

Fig. 7 Ge peak height compared to that of Si in EDX spectra obtained at different tilt conditions as a function of (a) tilt from [01-10] along 0001, (b) tilt from [12-30] along 0001, and (c) tilt from [01-10] along –2110.

Results and discussion

Annealing at 1200°C

Figures 1a and 1b show dark- and bright-field images of Ge-implanted 6H-SiC. Contrast variations due to strain form three distinct regions (marked I, II, and III). An EDX chemical profile for Ge, obtained along the dashed line marked in Fig. 1b, is shown in Fig. 1c. The profile shows that region III contains no detectable Ge, and so the observed strain contrast may be associated with the presence of point defects alone [13]. Figure 2a shows a [11-20] HR image of the complex defect structure present in the region marked with a white rectangle in Fig. 1b. In the 01-10 dark-field image in Fig. 2b, which was obtained from the same region, the defect structure is seen to consist of elongated stripes parallel to (0001).

Figures 3 and 4 show the results of Bloch wave calculations that were carried out to determine the excitations of atoms on lattice and interstitial sites for ALCHEMI. [01-10] and [12-30] zone axis incidences were found to show strong differences in excitation between lattice and interstitial sites, and to be within the tilt range of the goniometer used. Figures 3a, 3b, 4a and 4b show the projected structure and potential of 6H-SiC along [01-10] and [12-30], respectively. Figures 3c–e and 4c–e show electron-density distributions for Bloch waves corresponding to branches 1, 12, and 13, respectively. The electron density in branch 1 is concentrated on rows of Si atoms (Figs 3c and 4c) that in branch 12 is concentrated strongly on C and weakly on Si (Figs 3d and 4d), and that in branch 13 (Figs 3e and 4e) is concentrated on interstitial sites. The excitation conditions are very similar at the two zone axes. The excitation amplitude is shown as a function of k_{xy} (the component of the incident wave vector along the c^* axis of 6H-SiC) for [01-10] in Fig. 5. The excitation of the interstitial branch (13) has a maximum at $k_{xy} = \pm 5 / 2\ g_{0006}$, when 0 0 0 15 is in a Bragg condition. Spectra obtained at this tilt angle are expected to distinguish between Ge located at interstitial and lattice sites. The Si signal was used as a reference to obtain a measure of the thickness-averaged electron density in the interstitial sites.

Figure 6a shows an EDX spectrum obtained at [01-10] from the region circled in Fig. 1a. Figure 6b shows the corresponding spectrum obtained with the 0 0 0 15 reflection excited. The change in Ge peak area between the two spectra is clear. Spectra were acquired by exciting the 0003, 0006, 0009, 0 0 0 12, 0 0 0 15, and 0 0 0 18 reflections in turn. In Figs 7a and 7b, the X-ray emission counts for Ge around [12-30] and [01-10], respectively, are related to those for Si as a function of crystal tilt. The Ge/Si ratio shows a significant increase at tilts above $3 / 2g_{0006}$. Figure 7c shows similar results obtained at [01-10] for a tilt towards [–2110] (perpendicular to the c^* axis). The Ge/Si count rate now shows no significant dependence on tilt angle and thus no preferred channelling condition for lattice and interstitial sites. (No significant change in Ge/Si ratio was measured when tilting parallel to the c^* axis in region II of Fig. 1. In this region, the distortion of the matrix lattice disturbs the preferred channelling conditions.) Qualitatively, Figs 7a and 7b show that some Ge is localized on interstitial sites, in qualitative agreement with the calculation shown in Fig. 5. The fact that the measured variation is smaller than expected may be attributed to a decrease in peak intensity with tilt due to the orientation of the specimen holder with respect to the EDX detector. Channelling effects may also be diminished by

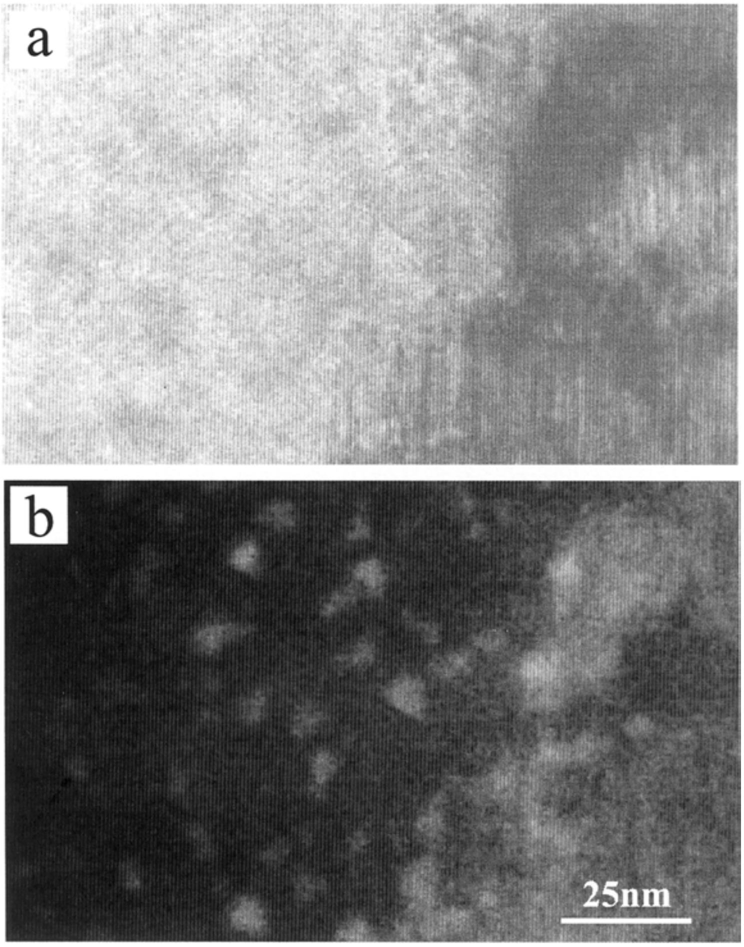

Fig. 8 (a) Bright-field STEM and (b) dark-field STEM images of the sample annealed at 1600°C from a depth region corresponding to the white rectangle in Fig. 1b, showing only in (b) contrast changes of regions around 10 nm in size.

Table 1 Dot's lattice parameters and inferred Ge content with following d-values

	$d_{measured}$ (nm)	Angle between planes (degrees)	Inferred Ge concn (vol%) with following d (nm)
Dot 1 (Fig. 10a)	$d_{111} = 0.325 \pm 0.003$		80–100
			$d_{111} = 0.324–0.3266$
Dot 2 (Fig. 10b)	$d_{111} = 0.320 \pm 0.005$	<(11-1), (-111)>:	70–100
	$d_{200} = 0.280 \pm 0.005$	70 ± 0.5	$d_{111} = 0.323–0.3266$
		<(11-1), (200)>:	
		55.0 ± 0.5	
Dot 3 (Fig. 10c)	$d_{\{01\text{-}10\}} = 0.331 \pm 0.005$	<{01-10} types>	70–100
	$d_{-\{12\text{-}10\}} = 0.193 \pm 0.005$	60.0 ± 0.5	$d_{01-10} = 0.337–0.3476$
Dot 4 (Fig. 10d)	$d_{111} = 0.331 \pm 0.003$	<{01-10} types>	–
		60.0 ± 0.5	
Dot 5 (Fig. 10e)	$d_{111} = 0.331 \pm 0.003$	<{01-10} types>	–
		60.0 ± 0.5	
Dot 6 (Fig. 10f)	$d_{111} = 0.314 \pm 0.003$	<(11-1), (-111)>:	below resolution limit
	$d_{220} = 0.275 \pm 0.001$	71.7 ± 0.6	
		<(11-1), (200)>:	
		54.0 ± 0.2	
Dot 7 (Fig. 10g)	$d_{111} = 0.312 \pm 0.003$		below resolution limit

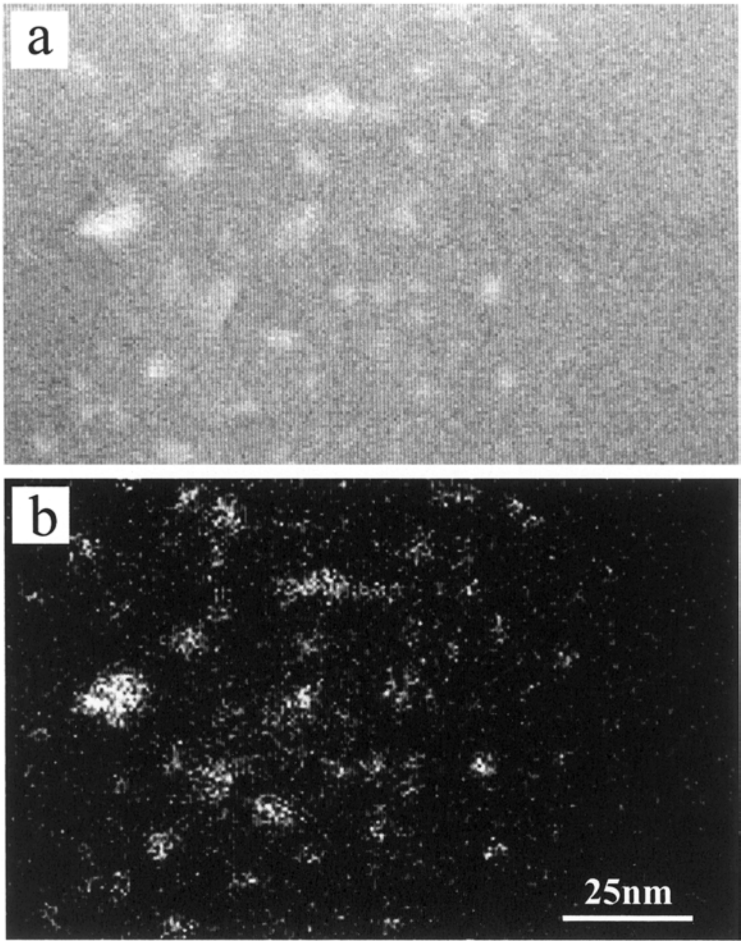

Fig. 9 (a) Dark-field STEM image and (b) Ge EDX map of the same region, showing a one-to-one correlation of high Ge content in (b) with bright regions in (a).

absorption and inelastic scattering [27], as well as by statistical disorder in the occupancy of lattice and interstitial sites.

Annealing at 1600°C

After annealing at 1600°C, the maximum in the Ge X-ray count rate distribution remains about the same as at the lower annealing temperature. Images obtained from an area equivalent to region I in Fig. 1a show that 3–10 nm sized nanocrystals are now present. HR images of the nanocrystals can only be obtained from the very thinnest regions of the TEM foil. Little contrast is seen in the bright-field STEM image in Fig. 8a, which was obtained at the position of the white rectangular box in Fig. 1b. Figure 8b shows that HAADF imaging [28] provides clearer contrast changes. However, the image is rather blurred due to a thick amorphous layer on top of the TEM foil. In Fig. 9, these contrast changes correlate well with the presence of Ge determined from EDX maps.

Table 2 Lattice parameter and interplane distances for Ge and Si in cubic and hexagonal notation

	Cubic Fd-3m	Corresponding hexagonal notation
Ge	a = 0.56576 nm	a = 0.40135 nm
	d_{111} = 0.3266 nm	d_{0001} = 0.3266 nm
	d_{220} = 0.2000 nm	$d_{01\text{-}10}$ = 0.34758 nm
Si	a = 0.54309 nm	a = 0.384023 nm
	d_{111} = 0.31355 nm	d_{0001} = 0.31355 nm
	d_{220} = 0.19201 nm	$d_{01\text{-}10}$ = 0.33257 nm

Several nanocrystals were studied using HR imaging in combination with EDX and EELS point analyses. Figure 10 shows HR images of three representative nanocrystals. The foil thickness was determined to be 30–50 nm in Fig. 10a, 80–110 nm in Fig. 10b and 40–70 nm in Fig. 10c by analysing EELS spectra using the log-ratio method [29]. EDX point analyses of the crystals and the adjacent matrix showed that the Ge contents of the dots are 80–100 vol% in Fig. 10a, 70–100 vol% in Fig. 10b and 70–100 vol% in Fig. 10c (Table 1), on the assumption that the thickness of each dot is the same as its width. In Fig. 10a, power spectra revealed a dominant lattice spacing in the crystal of 0.324 ± 0.003 nm at 14.9 ± 0.4° to 0004, which is close to the (111) spacing of Ge (Table 2). The

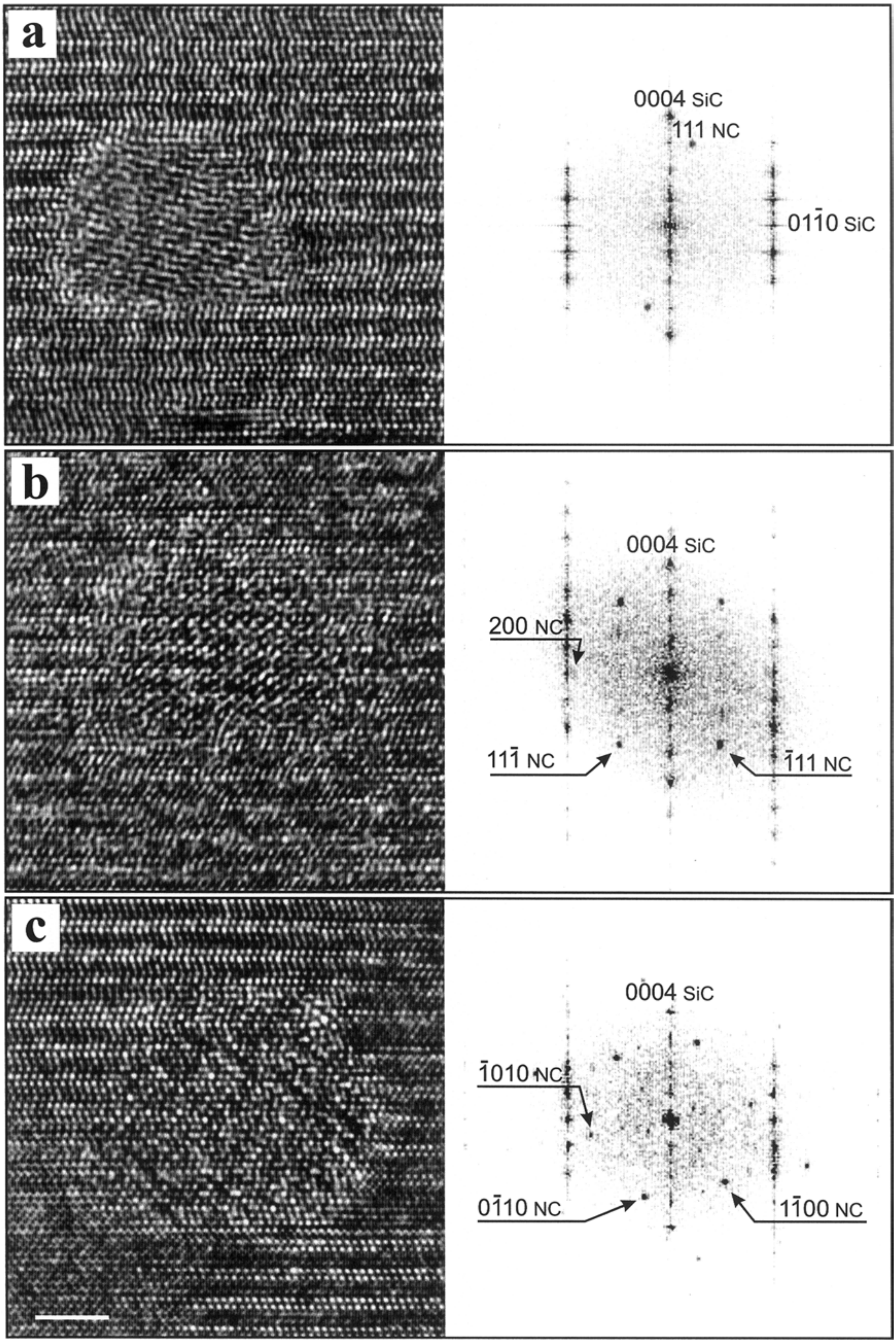
a
0004 SiC
111 NC
$01\bar{1}0$ SiC
b
0004 SiC
200 NC
$11\bar{1}$ NC
$\bar{1}11$ NC
c
0004 SiC
$\bar{1}010$ NC
$0\bar{1}10$ NC
$1\bar{1}00$ NC

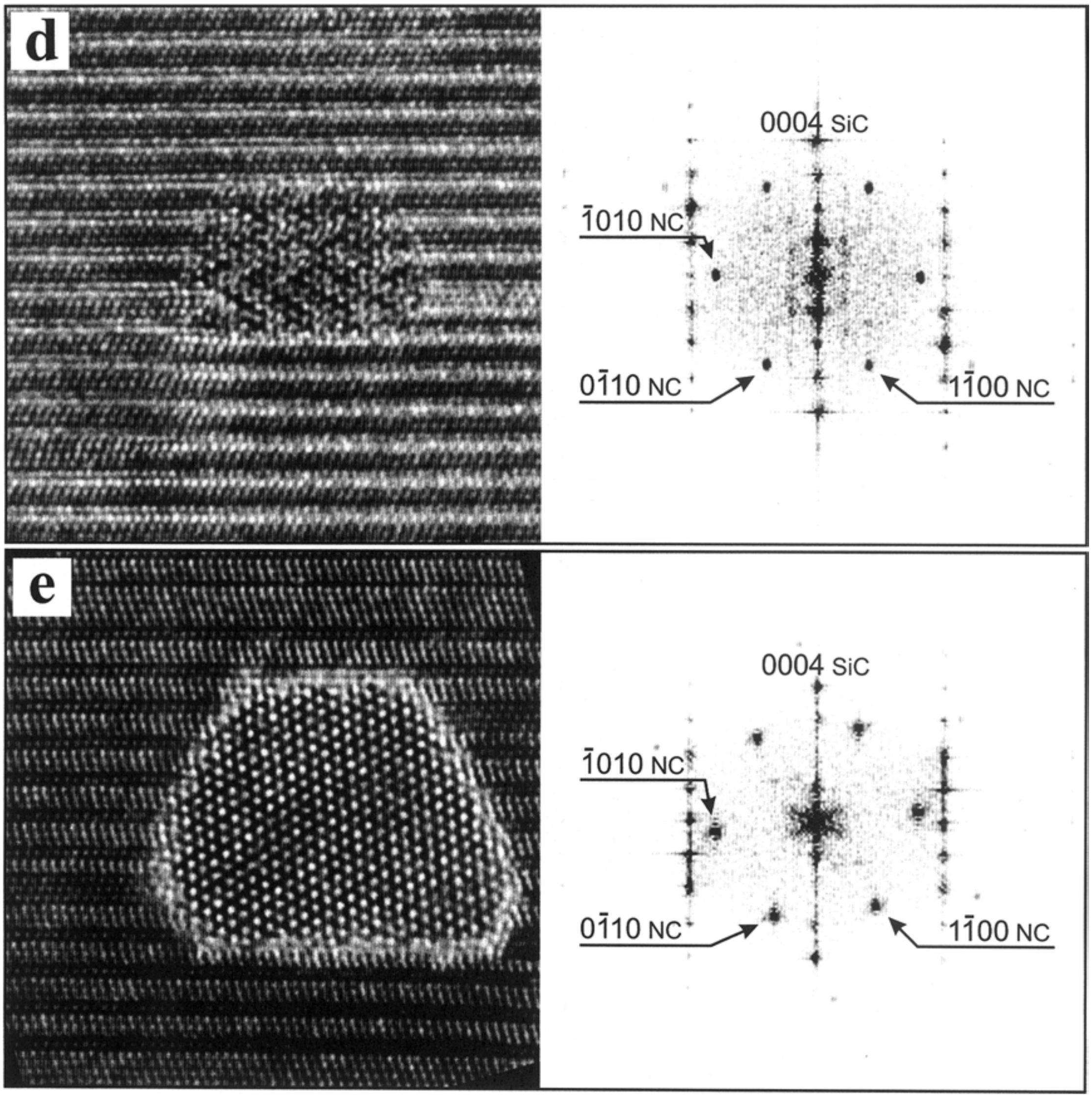

crystal in Fig. 10b contains two lattice spacings of 0.320 ± 0.005 nm that are symmetrical about 0004 and separated by 71.0 ± 0.5°. A further weak reflection (marked by the left arrow) most likely results from double diffraction [30]. This crystal is oriented along [01-1] with 200_{Ge} // $0\text{-}110_{SiC}$ and $0\text{-}22_{Ge}$ // 0004_{SiC}. The crystal in Fig. 10c contains 6 lattice spacings of 0.331 ± 0.005 nm that are 60.0 ± 0.5° apart and form an angle of 25.4 ± 1.0° with the 0004 reflection of SiC. However, this pattern is unlikely to correspond to the [111] zone of a cubic crystal lattice, as the corresponding lattice constant would be too high [17]. Figures 10d and 10e show that it is possible for the crystal in Fig. 10c to rotate around the 3-fold rotation inversion axis of the dots (Table 1).

Cell parameters and lattice spacings for Si and Ge are listed in Table 2. (Si and Ge are known to be continuously soluble [31].) The crystal in Fig. 10a is almost certainly close to being pure Ge, that in Fig. 10b is likely to be cubic Ge Si, while that in Figs 10c–e is likely to be strained hexagonal Ge or strained hexagonal Ge Si with its c-axis perpendicular to the c-axis of the SiC matrix. EDX spectra obtained from the crystals shown in Figs 10f and 10g did not reveal the presence of detectable Ge (Table 1). These crystals, which appear more rarely, may be interpreted as faulted Si oriented parallel to the SiC matrix with 0004 SiC // 111 Si and 11-20 SiC // 110 Si. If the stacking sequence in Figs 10f and 10g were to be repeated, 10H-SiC (Fig. 10f) and 17R-SiC (Fig. 10g) would result. HR image simulations confirm the fact that lattice fringes that are traditionally forbidden in the diamond structure may be present in the nanocrystals. For example, in Fig. 11, a simulated image of a 5 nm thick 2H-Ge nanocrystal viewed along [0001] is inserted into the image shown in Fig. 10e, and provides the observed extra reflections. Transformations from cubic to hexagonal Si similar to those observed experimentally here have been reported elsewhere [32,33]. The smallest (2.5 nm diameter) Ge-containing crystal imaged is shown in Fig. 12. Such crystals may be expected to show significant quantum effects [3].

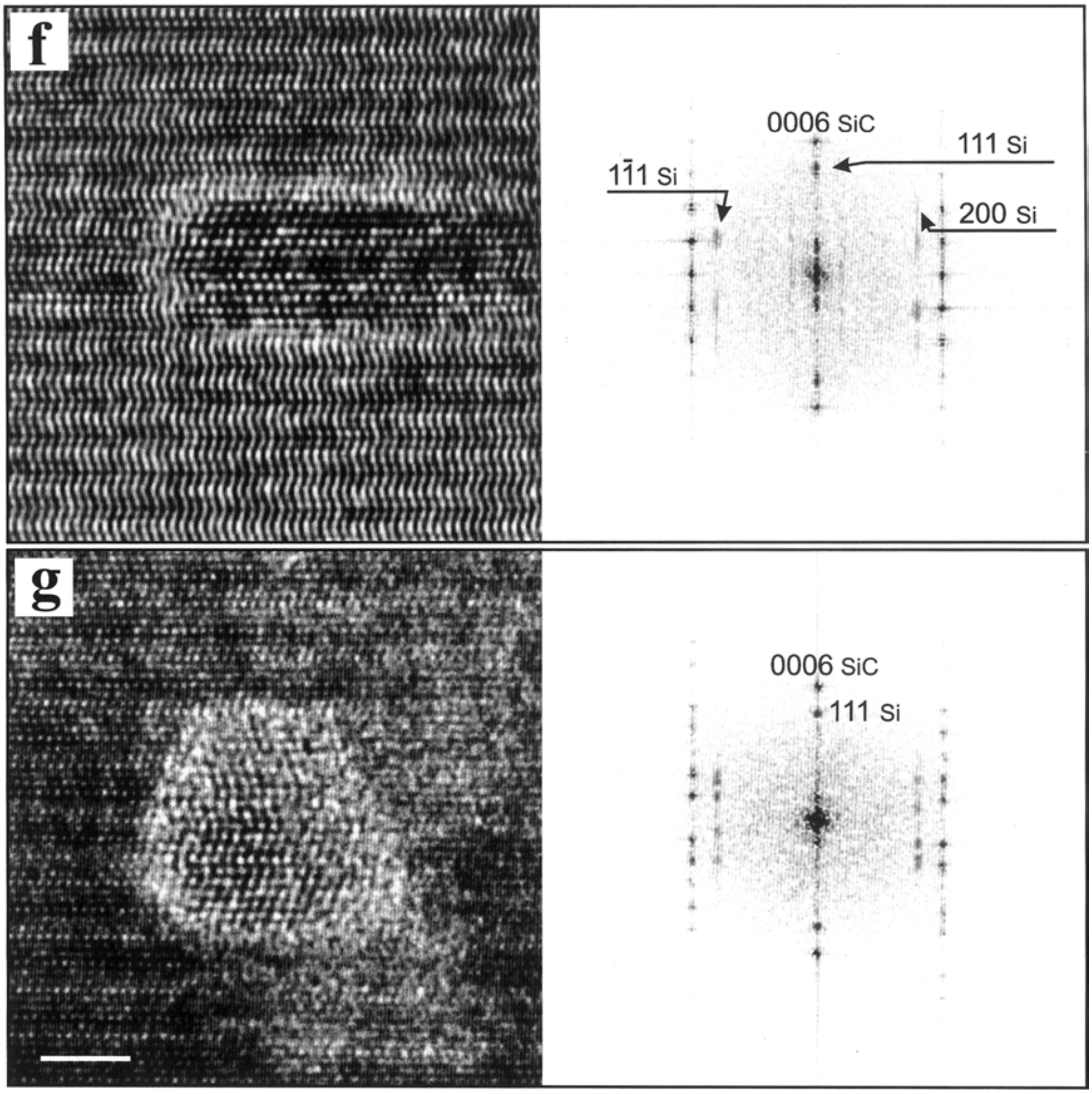

Fig. 10 HRTEM images of nanocrystals formed after annealing at 1600°C viewed along [11-20] of the hexagonal SiC matrix (4H-SiC for (a)–(f) and 6H-SiC for (g)). In (a)–(c), three typical Ge-containing nanocrystals are shown together with their FFT patterns. In (d) and (e), two different examples of the type of crystal in (c) are shown, demonstrating the possibility of rotation around its c-axis. In (f) and (g), two Si nanocrystals with the corresponding FFTs are shown. Both crystals are oriented parallel to the hexagonal matrix.

The above observations show that the collision cascades that accompany the implantation of Ge^+ atoms produce a high density of point defects (Si and C interstitials, vacancies) in the SiC matrix, as well as more complex defect clusters. Ge nanocrystals form in region I (Fig. 1a), where part of the Ge is located at interstitial positions before high temperature annealing. The bright stripes seen in Fig. 2b may be associated with small plate-like regions of high Ge content. About 5% only of the Ge present in this region should then be collected in such plates (see EDX profile in Fig. 1c). Therefore obviously Ge should also be distributed statistically on interstitial positions. After annealing at 1600°C, the diffusion of displaced atoms becomes increasingly likely and both defect annihilation and new defect (nanocrystal and void) formation can result. There is also a strong driving force for Si and C atoms to return to the SiC lattice [34]. A stable GeC lattice has not been reported in the literature, and so enhanced diffusion of Ge may produce more Ge atoms on interstitial positions and new Ge nanocrystals. Because Si and Ge can interdiffuse [35], it is likely that Si-Ge intermixed crystals form.

Concluding remarks

The microstructure of Ge-implanted hexagonal SiC has been studied after annealing at 1200 and 1600°C. After low temperature annealing, Ge occupies interstitial positions in the SiC matrix. After annealing at 1600°C, Ge-rich nanocrystals form. These nanocrystals comprise strained cubic and hexagonal Ge

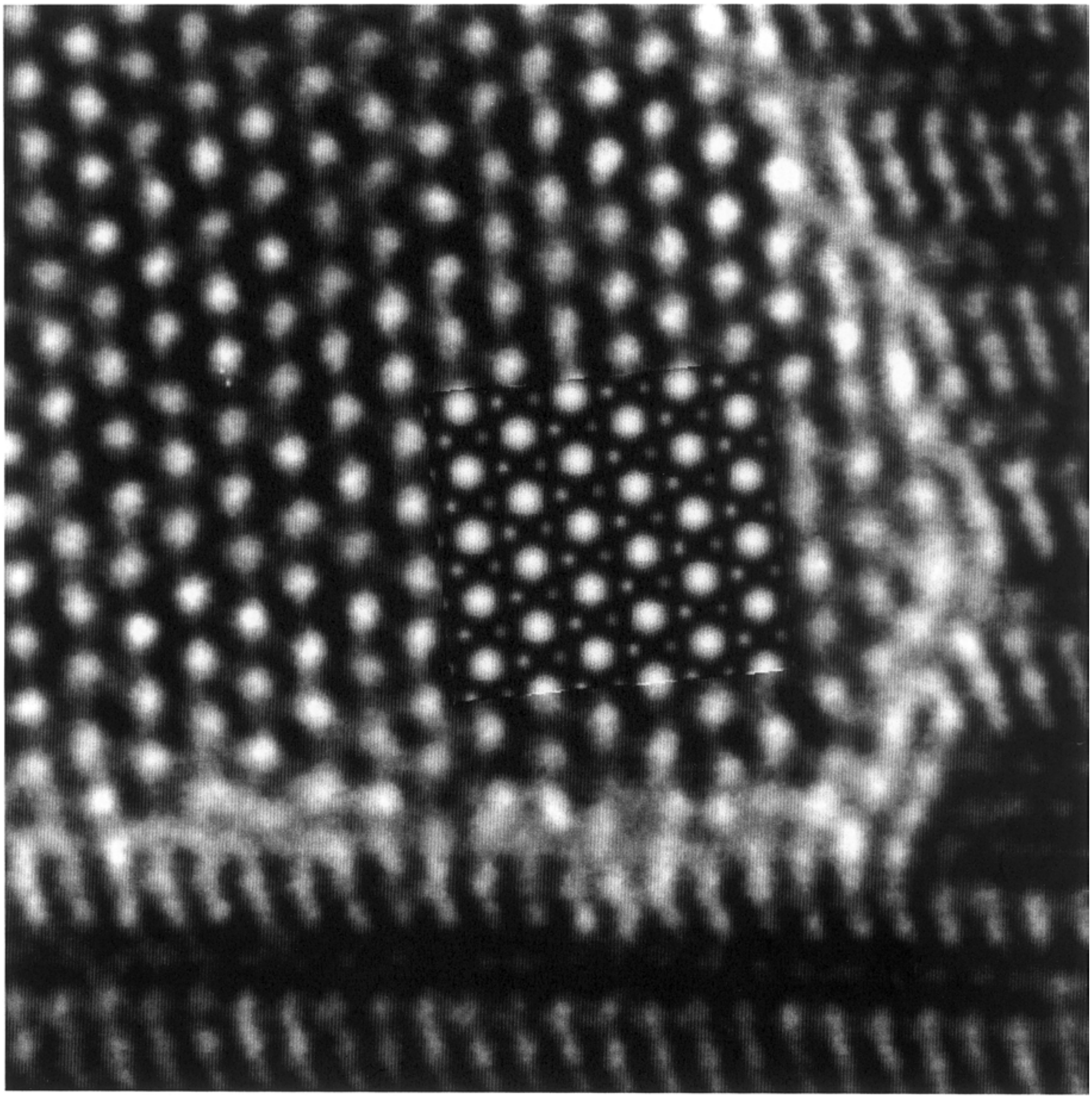

Fig. 11 Simulated HR image of a 5 nm thick 2H-Ge nanocrystal viewed along [0001] inserted in a detail of Fig. 10g showing the observed extra planes.

Si whose c-axis is parallel, inclined or perpendicular to the c-axis of the matrix. Occasionally, hexagonal Si nanocrystals with c-axes parallel to the c-axis of the SiC-matrix are observed also.

Acknowledgements

The author is deeply indebted to Prof. M. Tanaka, Dr. K. Saitoh and Dr. K. Tsuda for their generous scientific support during the ALCHEMI work including Bloch wave calculations, which were carried out as part of a JSPS fellowship at Tohoku University, both for encouraging discussions and experimental assistance. Particular thanks go to Dr. A. Chuvilin for common experimental work during his stay as a guest scientist at Jena University. The author is grateful to Prof. W. Wesch and Ch. Schubert for Ge ion implantation, Prof. D. Cockayne and Dr. R. Dunin-Borkowski for related experiments carried out in Oxford, Dr. M. Kawasaki from JEOL (Tokyo) for carrying out the HAADF experiment, Prof. Dr. Elke. Koch for discussions, Prof. U. Glatzel for uncomplicated access to the TEM and Prof. W. Richter for his interest. Special thanks go to Dr. R. Dunin-Borkowski for careful reading of the manuscript. The SFB 196 and JSPS ID No RC 29915003 supported this work.

References

1 Pavebi L, DalNegro L, Mozzoleni C, Franco G, and Priolo F (2000) Optical gain in Si nanocrystals. *Nature* **408**: 440–445.

2 Bisi O, Ossicini S, and Pavesi L (2000) Porous silicon; a quantum stonge structure for silicon based optoelectronics. *Surface Sci. Rep.* **38**: 1.

3 Takagahara T and Takeda K (1992) The theory of quantum confinement effect on excitons in quantum dots of indirect-gap materials. *Phys. Rev. B* **46**: 15578–15585.

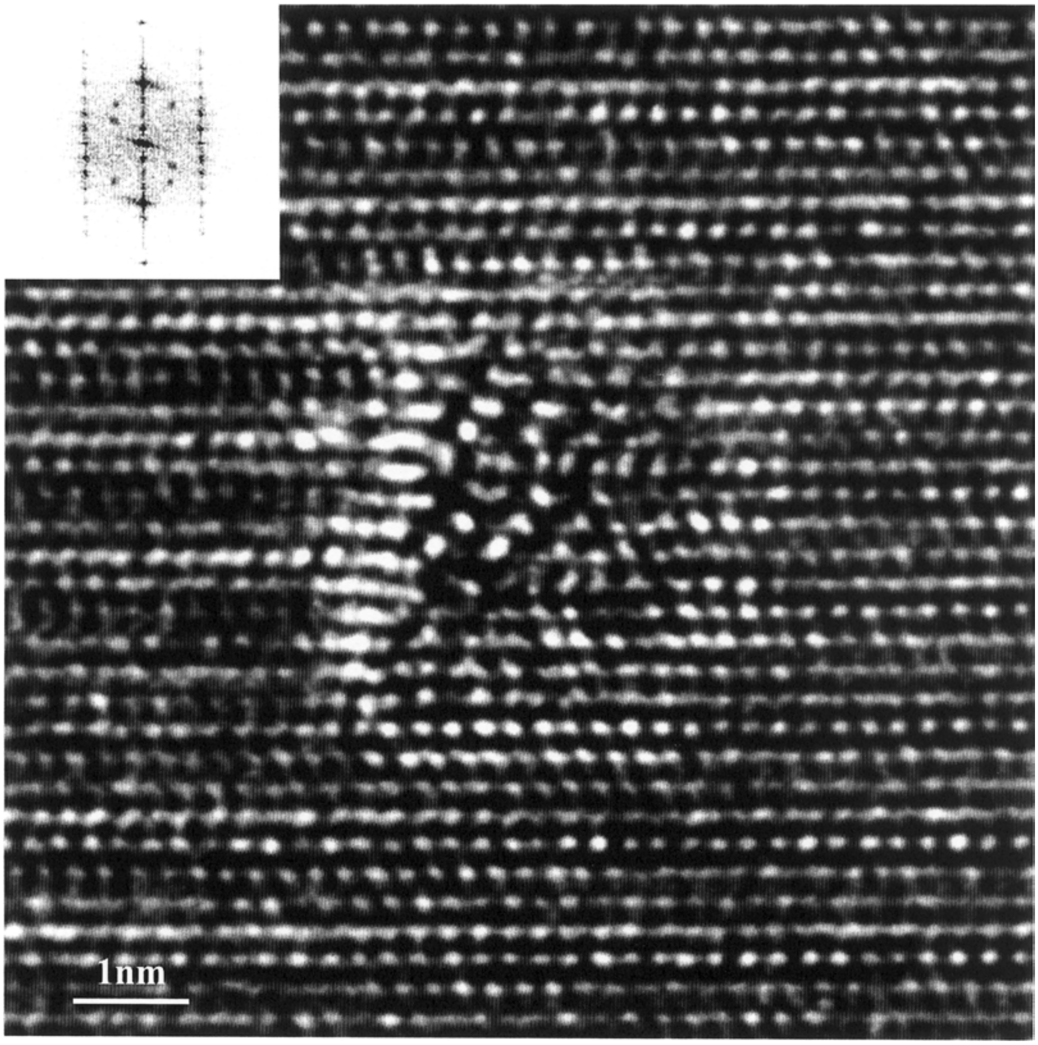

Fig. 12 HRTEM image of a small Ge-containing nanocrystal formed after annealing at 1600°C, viewed along [11-20] of 4H-SiC.

4 Takeoka S, Fujii M, Hayashi S, and Yamamoto K (1998) Size dependent near infrared photoluminescence from Ge nanocrystals embedded in the SiO_2 matrices. *Phys. Rev. B* **58**: 7921–7925.

5 Katulka G, Guedj C, Kolodzey J, Wilson R G, Swann C, Tsao M W, and Rabolt J (1999) Electrical and optical properties of Ge-implanted 4H-SiC. *Appl. Phys. Lett.* **74**: 540–542.

6 Fissel A, Schröter B, Kaiser U, and Richter W (2000) Advances in the molecular-beam epitaxial growth of artificially layered heteropolytypical structures of SiC. *Appl. Phys. Lett.* **77**: 2418–2420.

7 Lindner J and Stritzker B (1999) Controlling the density distribution of SiC nanocrystals for the ion beam synthesis of buried SiC layers in silicon. *Nucl. Instrum. Methods B* **147**: 249–255.

8 Bechstedt F (2001) Private communication.

9 Watkins G D (1968) *Radiation Effects on Semiconductors*. (Plenum Press, New York.)

10 Fedina I L and Aseev A (1986) Study of interaction of point defects with dislocations in silicon by means of irradiation in an electron microscope. *Phys. Stat. Sol. A* **95**: 517–523.

11 Lebedev O I, Van Tendeloo G, Suvorova A A, Usov I O, and Suvorov A V (1997) HREM study of ion implantation in 6H-SiC at high temperatures. *J. Electron Microsc.* **46**: 271–279.

12 Ohno T and Kobayashi N (1999) Secondary defect distribution in high energy ion implanted 4H-SiC. *Mat. Sci. Forum* **338–342**: 913–916.

13 Heera V, Stoemenos J, Kögler R, and Skorupa W (1995) Amorphization and recrystallization of 6H-SiC by ion-beam irradiation. *J. Appl. Phys.* **77**: 2999–3009.

14 Yoo W S and Matsunami H (1991) Solid-state phase transformation in cubic silicon carbide. *Jpn. J. Appl. Phys.* **30**: 545–553.

15 Suttrop W, Zhang H, Schadt M, Pensl G, Dohuke K, and Leibenzeder S (1992) Recrystallisation and electrical properties of high temperature implanted (N, Al) 6H-SiC layers. *Springer Proc. Phys.* **71**: 143–147.

16 Jäger C H, Jäger W, Pöpping J, Bösker G, and Stolwijk N A (2000) Formation of metal precipitates and voids by zinc diffusion in GaP. *J. Electron Microsc.* **48**: 1037–1046.

17 Gorelik T, Kaiser U, Glatzel U, Schubert C H, and Wesch W (2001) A TEM study of Ge implantation into SiC. *J. Mater. Res.* (submitted).

18 Lhermitte-Sebire I, Vicens J, Chermant J L, Levalois M, and Paumier E (1994) Transmission electron microscopy and high-resolution electron microscopy studies of structural defects induced in 6H-SiC single crystals irradiated by swift Xe ions. *Phil. Mag. A* **69**: 237–244.

19 Föhl A, Emrick R M, and Castanjen H D (1992) A Rutherford back scattering study of Ar- and Xe-implanted silicon carbide. *Nucl. Instrum. Methods B* **65**: 335–346.

20 Guedj C and Kolodzey J (1999) Substitutional Ge in 3C-SiC. *Appl. Phys. Lett.* **74**: 691–693.

21 Wendler E, Heft A, and Wesch W (1998) Ion-beam induced damage and annealing behaviour in SiC. *Nucl. Instrum. Methods B* **141**: 105–109.

22 Pacaud V, Skorupa W, and Stoemenos J (1996) Microstructural characterization of amorphized and recrystallized 6H-SiC. *Nucl. Instrum. Methods B* **120**: 181–185.

23 Tsuda K and Tanaka M (1999) Refinement of crystal structural parameters using two-dimensional energy-filtered CBED patterns. *Acta Cryst.* **A55**: 939–954.

24 Doyle P A and Turner P S (1968) Relativistic Hartree-Fock X-ray and electron scattering factors *Acta Cryst* **A24**: 390–397.

25 *User Manual, Digital Micrograph*. (Gatan, Inc., Pleasanton, CA.)

26 Ruijter W J, Sharma R, McCarter M R, and Smith D J (1991) Measurement of lattice-fringe vectors from digital HREM images: experimental precision. *Ultramicroscopy* **57**: 409–422.

27 Buseck P R (1993) *Minerals and Reactions at the Atomic Scale: Transmission Electron Microscopy.* (Mineral. Soc. Amer., Washington, DC).

28 Pennycook S J and Jesson D E (1991) High-resolution Z-contrast imaging of interfaces. *Ultramicroscopy* **37**: 14–38.

29 Egerton R F (1999) *Electron Energy-Loss Spectroscopy in the Electron Microscope.* (Plenum Publishing Corp.)

30 Williams D B and Carter C B (1996) *Transmission Electron Microscopy.* (Plenum Press, New York.)

31 Lide D R (1997) *Handbook of Chemistry and Physics*. (CRC Press.)

32 Yeh C, Lu Z W, Froyen S, and Zunger A (1992) Zinkblende-Wurzit polytypism in semiconductors. *Phys. Rev. B* **46**: 10086–10097.

33 Tan T Y, Föll H, and Hu S M (1981) On the diamond-cubic to hexagonal phase transformation in silicon. *Phil. Mag. A* **44**: 127–140.

34 Taylor A and Jones R M (1960) *Silicon Carbide.* (Pergamon Press, Oxford.)

35 Boscherini F, Capellini G, Di Gaspare L, De Seta M, Rosei F, Sgarlata A, Motta N, and Mobilio S (2000) Ge-Si intermixing in Ge quantum dots on Si. *Thin Solid Films* **380**: 173–175.